

Thrust and Power Output of the Bacterial Flagellar Motor: A Micromagnetic Tweezers Approach

Christopher J. Pierce, Emily Osborne, Eric Mumper, Brian H. Lower, Steven K. Lower, and Ratnasingham Sooryakumar^{1,*}

¹Department of Physics, ²School of Environment and Natural Resources, ³School of Earth Sciences, and ⁴Department of Microbial Infection and Immunity, The Ohio State University, Columbus, Ohio

ABSTRACT One of the most common swimming strategies employed by microorganisms is based on the use of rotating helical filaments, called flagella, that are powered by molecular motors. Determining the physical properties of this propulsive system is crucial to understanding the behavior of these organisms. Furthermore, the ability to dynamically monitor the activity of the flagellar motor is a valuable indicator of the overall energetics of the cell. In this work, inherently magnetic bacteria confined in micromagnetic CoFe traps are used to directly and noninvasively determine the flagellar thrust force and swimming speed of motile cells. The technique permits determination of the ratio of propulsive force/swimming speed (the hydrodynamic resistance) and the power output of the flagellar motor for individual cells over extended time periods. Cells subjected to ultraviolet radiation are observed to experience exponential decays in power output as a function of exposure time. By noninvasively measuring thrust, velocity, and power output over time at a single-cell level, this technique can serve as the foundation for fundamental studies of bacterial hydrodynamics and also provides a novel, to our knowledge, tether-free probe of single-cell energetics over time.

SIGNIFICANCE Many bacterial species navigate their surroundings by rotating one or more molecular-motor-driven external appendages, called flagella. This study presents a noninvasive measure of the flagellar force exerted by individual cells, employing a class of inherently magnetic bacteria. By tuning magnetic confinement forces on individual cells, the strength of the flagellar force is deduced, revealing fundamental aspects of their swimming mechanics, cell-to-cell variations over time, and responses to cellular damage such as exposure to ultraviolet radiation. Monitoring flagellar activity reveals critical aspects of swimming behavior and serves as a valuable time-resolved probe of single-cell metabolism. Furthermore, the technique introduced in this study may be readily extended to other, nonmagnetic swimming microorganisms.

INTRODUCTION

Bacteria represent a large fraction of the Earth's biomass (1–4) and can dramatically affect human health outcomes (5–7), serve as the foundation of ecosystems (8–12), and even alter the chemical and physical geology of the planet (13–16). Motility and chemotaxis (17–22)—the ability to selectively navigate a chemically heterogeneous microenvironment—are essential to the viability of many bacterial species. Central to this motility is a chemically driven helical appendage known as the flagellum (23), which serves as the source of bacterial propulsion. Gaining insight into

Submitted May 13, 2019, and accepted for publication August 30, 2019.

*Correspondence: sooryakumar.1@osu.edu

Editor: Philip LeDuc.

https://doi.org/10.1016/j.bpj.2019.08.036

© 2019 Biophysical Society.

flagellar thrust and the resulting hydrodynamics that determine swimming trajectories is not only crucial to understanding the behavior of these organisms but also to the development of analogous synthetic and biohybrid microswimmers (24,25) and the realization of biology-driven nanomedicine (26). Moreover, flagellar propulsion is also the source of activity in a broad class of active matter systems (27,28), displaying diverse collective behaviors far from equilibrium, including self-assembled clusters (29-31), vortices (32,33), and pearling structures (34). Finally, flagellar activity serves as a proxy for the overall cellular energetics, making the power output of the flagellar motor a valuable quantity for investigations of single-cell metabolics (35). Despite the relevance of flagellar thrust to these diverse areas, only a limited number of techniques (36,37) permit in situ measurement of flagellar thrust and



related physical properties of flagellated microswimmers. These techniques rely on either optical-tweezers-based approaches (37) or dielectrophoresis (36), which do not readily permit repeated measurements on individual cells and offer substantial challenges to scaling the cell throughput.

In this work, we present a novel, to our knowledge, means of directly measuring the flagellar thrust output by the flagellar motors of large numbers of bacteria, using a micromagnetic platform (38) and an inherently magnetic model swimmer, the amphitrichous (biflagellated) magnetotactic bacterium Magnetospirillum magneticum (AMB-1) (39) (Fig. 1 a). Exploiting their magnetism by applying forces and torques to the cell body allows direct measurement of the flagellar thrust, swimming speed, and magnetic moment of each individual cell, which in turn enables direct calculation of the hydrodynamic resistance and overall power dissipated by the flagellum. Finally, the exploitation of this technique for single-cell metabolic experiments is demonstrated by noninvasively tracking the decay of flagellar output power under exposure of the cell to ultraviolet (UV) radiation. This approach permits direct, tether-free monitoring of the flagellar activity of single cells for extended periods of time, and furthermore, because the technique is

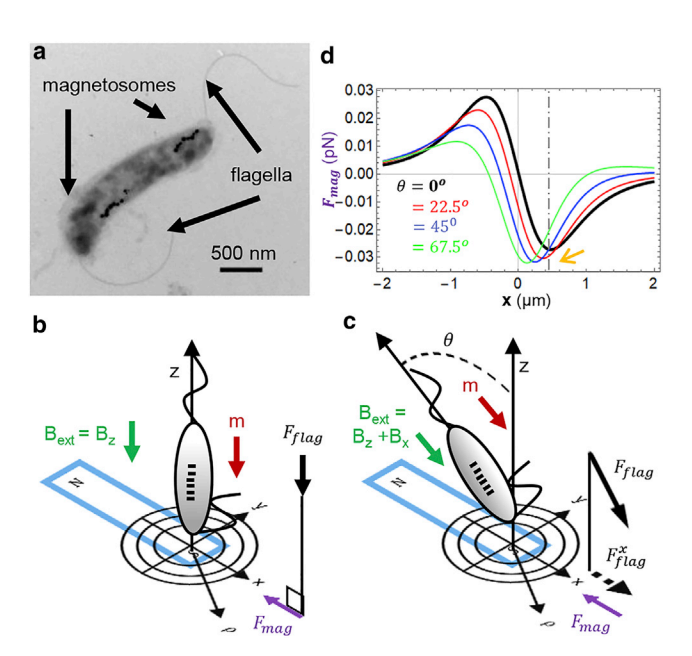


FIGURE 1 (a) TEM image of AMB-1 showing magnetosome chain and flagella. (b) A cell is trapped over the south pole of a CoFe micro-bar magnet under the influence of an external magnetic field pointing into the surface $(B_{ext} = B_z)$. In this condition, flagellar forces F_{flag} act in the z-direction while magnetic trap forces F_{mag} act in the plane and orient toward the center of the trap (circular contours indicate lines of constant force). (c) When the cell is tilted along the long axis of the bar magnet (x-direction) with an inplane field $(B_{ext} = B_z + B_x)$, a flagellar force component F_{flag}^{xy} is projected into the plane, and $F_{\it mag}$ is attenuated, allowing the relative strength of $F_{\it flag}$ and F_{mag} to be tuned until, at a critical angle θ_c , the cell escapes the trap. (d) F_{mag} along the x-direction is shown, calculated as a function of external field angle θ . The force barrier increases and moves away from the trap center as θ is increased. To see this figure in color, go online.

based on lithographic techniques developed in the semiconductor industry, it suggests a route to high-throughput scaling of single-cell studies through multiplexing.

MATERIALS AND METHODS

AMB-1 cells derive their inherent magnetism from internal membranebound nanoparticles, called magnetosomes (40). They also possess two antipodal flagella (41) that allow them to swim parallel or antiparallel to magnetic field lines, thereby allowing their swimming direction to be controlled by a homogeneous external magnetic field-magnetic torque applied to the magnetosomes causes the cell body and flagellar thrust to align with the chosen field direction. Alternatively, to apply magnetic forces requires spatial gradients in the magnetic field. To create such gradients, microscopic linear cobalt-iron (CoFe) microstructures are patterned onto a surface (see Fig. 1) (38). These micro-bar magnets are initially magnetized by a momentary large (~10,000 G) external field that produces a single-domain magnet. Upon removal of this initial field, the domains relax into a "bar magnet" state, wherein the central segment is largely homogeneously magnetized, whereas at the termini, domain walls emerge that act as either a local source (north pole) or sink (south pole) of magnetic field. These poles produce sites with locally high field gradients (10⁴ T/m) (38), allowing forces comparable in scale to the flagellar thrust (~pN) to be applied on nearby AMB-1 cells under microscope observation. Images are recorded using a custom-built Leica Metallurgical Microscope (Leica Microsystems, Buffalo Grove, IL) in brightfield illumination using a $40\times$ objective and a Retiga-EXI camera (QImaging, Surrey, BC, Canada). Videos are recorded using Nikon Elements Software and analyzed in ImageJ. See Videos S1, S2, and S3 for recorded cellular trajectories and accompanying description for details of the experimental protocol.

As previously demonstrated (42), these patterned traps are capable of suppressing the movement of AMB-1 to achieve single-cell confinement. To trap a bacterium, its body is first oriented perpendicular to the patterned surface (Fig. 1 b) by a weak external field pointing into the surface $(B_z \sim -90 \text{ G})$ produced by a surrounding solenoid. This results in accumulation of cells with a given polarity (north-seeking) near the surface bearing the CoFe magnets, whereas cells of the opposite swimming polarity are driven away. When far removed from the CoFe magnets, these perpendicularly oriented cells drift laterally, like a top, while perpetually swimming into the solid surface. Near the magnetic patterns, however, the local field generates a magnetic force on the magnetosome chain. The patterned north poles become sites of repulsion, whereas south poles become sites of attraction, which draw the cell to the center of the bar terminus and suppress lateral (xy) position fluctuations, creating a trap.

Once the cell is located in the trap, an additional in-plane external field component (B_{ext}^{xy}) provided by a two-axis electromagnet (38) causes the external field and cell body to tilt away from the z axis and project a component of the flagellar thrust F_{flag}^{x} along the surface plane. Here, we have assumed that the mean cell orientation is well-aligned with the field. Although hydrodynamic torques can cause large discrepancies between the cell long axis and field orientation, these may be eliminated at large fields in which the magnetic torque overcomes hydrodynamic torques and thermal motion (42). Thus, for the field strengths used in this study (90 G), the mean cell orientation is taken to be parallel to the external field. As the tilt angle (θ) is increased from perpendicular (Fig. 1 c), F_{flag}^x increases relative to the magnetic trap force (F_{mag}) on the cell. Thus, just beyond a critical tilt angle θ_c where F_{flag}^x balances F_{mag} , the cell escapes the trap, allowing the flagellar thrust F_{flag}^x to be inferred from the known magnetic forces acting on the cell at its escape angle. For a magnetic cell with magnetic moment m, F_{mag} (plotted for several angles θ in Fig. 1 d) is given as

$$F_{mag} = m \left[\sin \theta \frac{\partial B_x}{\partial x} - \cos \theta \frac{\partial B_z}{\partial x} \right]. \tag{1}$$

Hence, determining F_{mag} (and thus F_{flag}) requires 1) a calibration of the trap achieved by measuring the field gradients in its vicinity, 2) acquisition of the magnetic moment m of each individual bacterium, and 3) determination of the angle of escape θ_c . Using this combination of measurements, the flagellar thrust F_{flag} and also swimming speed V_{cell} are determined from a single measurement sequence.

Trap calibration

Superparamagnetic beads (diameter $d=2.8~\mu m$ Dynabeads M-270 (Thermo Fisher Scientific, Waltham, MA)) of diameter comparable to the cell lengths are used to determine the field gradients emanating from the CoFe micro-bar magnets. Unlike AMB-1, which has a constant magnetic moment m, superparamagnetic beads have a magnetic moment proportional to the net field $m_{bead} = \chi_V V B_{tot}$ where χ_V is the particle volume susceptibility (0.17 for previously measured beads (43)) and V is the bead volume. Hence, the force on a superparamagnetic bead is given by

$$\vec{F}(\rho, z_0) = -\vec{V} \left(\vec{m} \cdot \left[\vec{B}_{CoFe}(\rho, z_0) + \vec{B}_{ext}(t) \right] \right) = -\chi_V V \mu_0 \vec{V} \left| \vec{B}_{CoFe}(\rho, z_0) + \vec{B}_{ext}(t) \right|^2.$$
 (2)

 B_{CoFe} is the field due to the CoFe micro-bar magnet, ρ is the horizontal distance of the bead to the trap center, z_0 the height of the bead center, B_{ext} is the uniform external magnetic field, and μ_0 is the permeability of free space. When $B_{ext}=0$, both north and south poles act as symmetric sites of attraction (traps) because the magnetic forces guide the superparamagnetic beads up the field gradients ($F(r)=-\chi_v V \, V \, B_{CoFe}^2(r)$) to sites of maximal field strength (the poles). When B_{ext} is sufficiently large and is oriented perpendicular to the surface, this symmetry is broken. For instance, when B_{ext} points into the surface, north poles become repulsive sites, whereas south poles become attractive. Conversely, out-of-plane external fields reverse this polarity. Thus, a bead may be repeatedly repelled and attracted to a given pole simply by flipping the z-component of B_{ext} , as illustrated in Fig. 2, a and b.

The bead's horizontal distance from the trap center $\rho(t)$ is recorded during such a repeated field sequence and the positions tracked in ImageJ using the Trackmate plugin, allowing the bead velocity, $v_{bead}(\rho)$, to be calculated as a function of the distance from the trap center. Because of the low Reynold's number of the system, the magnetic forces on the bead are directly proportional to v_{bead} , $(F_{bead} = Rv_{bead})$ where $R = 6\pi\eta d/2$ is the bead's hydrodynamic resistance (or drag constant). Thus, the bead velocity taken from the recorded trajectories allows the field gradients (VB_{CoFe}) emanating from the patterned magnet to be determined. By invoking a simplified magnetic point-charge model of $B_{CoFe}(r)$, the field from the south pole of the trap may be calculated (38):

$$\vec{B}_{CoFe} = k \frac{\hat{r}}{r^2},\tag{3}$$

where k is a constant quantifying the trap strength and $\vec{r} = \vec{\rho} + z_0 \hat{z}$ is the distance from the trap center. Under an external magnetic field $\vec{B}_{ext} = B_{ext} \hat{z}$, the magnetic force on a superparamagnetic particle along the in-plane ρ -direction is given as

$$F_{\rho}(\rho, z_0) = \gamma v_{bead}(\rho, z_0)$$

$$= -2\chi k \rho \left(\frac{2k + \frac{3}{2} z_0 \sqrt{\rho^2 + z_0^2} B_{ext}}{(\rho^2 + z_0^2)^{3/2}} \right), \tag{4}$$

where z_0 is the effective height of the particle above the plane of the pointcharge field source. Fitting the experimental bead velocity data to the above

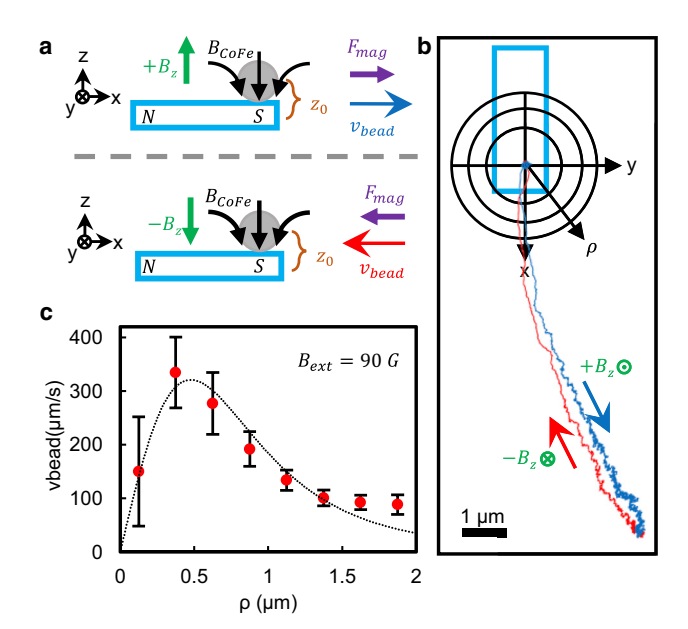


FIGURE 2 Trap calibration. (a) A schematic of the bead launch experiment at a south pole trap under negative (top) and positive (bottom) z-fields is given. (b) Bead launch trajectories under repulsion and attraction are shown. (c) Experimental bead velocity $v_{bead}(\rho)$ versus radial distance ρ from trap center for a single superparamagnetic bead repeated for six trials is shown. Solid line shows fit to magnetic point-charge model. To see this figure in color, go online.

model (Fig. 2c), all parameters (k, z_0) needed to calculate the field gradients associated with the micromagnetic trap are determined.

Determining the magnetic moment and flagellar thrust of AMB-1

AMB-1 cells are cultured in nitrogen-purged serum bottles on magnetic *Spirillum* growth media, which consists of medium 1653 from the American Type Culture Collection (Manassas, VA) with substitution of Frankel's vitamin solution and modified Wolfe's mineral solution (44). For the following experiments, small (μ L) samples are removed from the main culture and pipetted onto a substrate containing the calibrated magnetic patterns. The cell mixture is contained laterally by a piece of polydimethylsiloxane cut into the shape of an o-ring and sealed by a glass coverslip placed atop the o-ring.

To determine the escape angle θ_c , the cell is first guided to the trap center and trapped in a vertical (z-direction) orientation pointing into the surface. The tilt angle θ is then incrementally increased by increasing B_{vt}^{yy} in 10 G steps until the cell escapes the trap at the critical angle θ_c . Upon escape from the trap, the cell is then made to swim parallel to the surface by imposing an external field purely in the plane ($B_{ext}^z = 0$) to determine the cell swimming speed V_{cell} . To estimate the magnetic moment m, a u-turn experiment (45) is then performed. Once the cell has been guided away from any nearby trapping sites, rapid reversal of the direction of \vec{B}_{ext}^{yy} causes the cell to execute a "u-turn." By comparing the associated magnetic torque to the rotational drag f_r on the AMB-1 cell body, the measured time τ_u taken to complete the u-turn (45) may be related to m as follows:

$$m = \frac{f_r}{\tau_u B_{ext}}. (5)$$

The rotational drag coefficient f_r is approximated by the drag on a rod, given as (46)

$$f_r = \frac{8\pi\eta dl^2}{3\left[\ln\left(\frac{2l}{d}\right) - \frac{1}{2}\right]},\tag{6}$$

where l is the cell length (measured optically), $d = 1.2 \mu m$ is the effective cell diameter (minimal separation between two neighboring, oriented cells (31)), and η is the fluid viscosity.

The observed θ_c , along with the trap calibration information (k) and magnetic moment (m), are then used to calculate the flagellar thrust F_{flag} . This measurement sequence was applied to each cell in the study.

UV exposure

For the UV exposure experiments, the measurement sequence described above (yielding V_{cell} , m, and F_{flag}) was carried out repeatedly for a given cell over time. After each sequence was performed, in-plane fields were used to guide the cell of interest back to the calibrated micro-bar magnet. This process was repeated for an extended period ($\sim \! 10$ min) to establish the constancy of the flagellar thrust, velocity, and cell moment over time and to average over stochastic effects. Once a baseline set of measurements were acquired (~13 trials on average for each cell with an average SD of \sim 30%), the cells were then exposed to \sim 1 s pulses of UV radiation via a mercury halide lamp (Leica EL6000), operating at its maximal measured output intensity (\sim 96 mW/cm²) for \sim 20 min. After each UV pulse, an additional set of measurement sequences was performed to ascertain the effect of the pulse on the quantities of interest (V_{cell} and F_{flag}) for ~ 2 min after each pulse. After acquiring measurements for ~10 pulses, the UV lamp was left on to continually expose the cells. Under this constant exposure, the measurement sequence was repeated until the cell ceased to achieve the necessary thrust to escape the trap. The power output ($V_{cell} imes F_{flag}$) at each cumulative exposure time was then calculated by averaging over repeated trials collected during the pulse sequence or reported from single measurements in the case of the continuous exposure portion of the experiment. The experiment sequence is summarized schematically in Fig. 3.

RESULTS AND DISCUSSION

Thrust and hydrodynamic mobility

Fig. 2 illustrates results from a CoFe trap calibration experiment performed with $B_{ext} = 90$ G. The bead velocity $v_{head}(\rho)$ is based on a running average of $\rho(t)$ data and is compiled from six repeated trials. A fit (Fig. 2 c) to the magnetic point-charge model displays reasonable agreement to the data and reveals a trap strength of $k = 2.8 \pm 0.5$ G μm^2 and an effective distance ($z_0 = 0.95 \pm 0.06 \mu \text{m}$) between the point-charge field source and the bead. Discrepancies between the bead's response and the theoretical prediction likely arise from the finite size of the bead and the presence of higher-order (e.g., dipole, quadrupole) fields not accounted for by the point-charge model. Despite these effects, the model displays good agreement with the data near the point of maximal force (Fig. 2 c), which is most relevant to determining the magnetic force barrier the cell must overcome to escape and hence to the flagellar thrust.

Using the deduced trap parameters (k, z_0) , the flagellar thrust F_{flag} of 118 cells was determined by 1) successively navigating individual cells to the calibrated micro-bar-magnet trap, 2) launching them off by incrementally changing θ from 0° to 48° , 3) noting the angle of escape θ_c , and 4) immediately performing a u-turn sequence to determine the magnetic moment m and the in-plane swimming speed V_{cell} . Fig. 4 summarizes the distributions of m, V_{cell} , cell body length l, and flagellar thrust force (F_{flag}) for the 118 bacteria (see Videos S1, S2, and S3 showing measurement sequences).

The mean magnetic moment m, $0.87 \pm 0.34 \times 10^{-16}$ Am^2 , is roughly 2–10 times smaller than recently reported values for AMB-1 (42,45) but displays good agreement with other previously reported values (47–49). This variation may arise from differences in growth conditions The optically determined mean cell length $l = 2.7 \pm 0.5 \mu m$ is comparable to direct determination of cell lengths in transmission electron microscopy (TEM (39,45)) and the distribution of cell lengths reported in prior optical studies (45). Likewise, the mean velocity 18.3 μ m/s of this bacterial population is consistent with earlier studies of AMB-1 (42). The measured mean thrust of the population of 0.029 pN shown in Fig. 4 d is an order of magnitude smaller than the thrust determined in studies on Escherichia coli (0.57

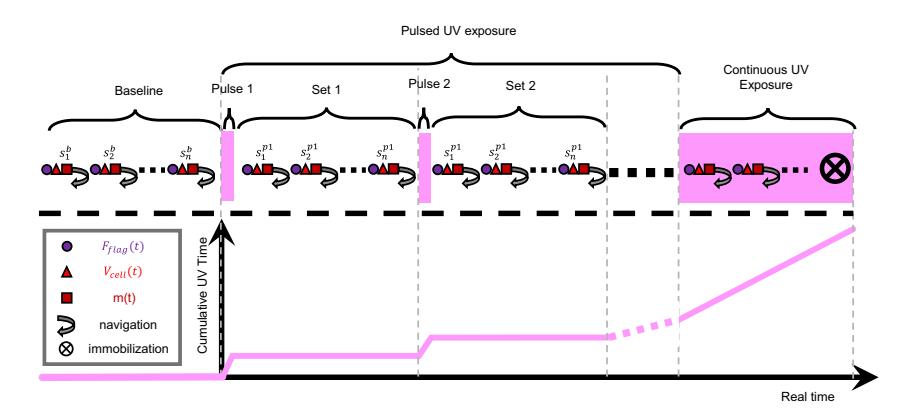


FIGURE 3 Schematic illustration of UV experiment. Measurement sequences s are shown that produce F_{flag} (circles), V_{cell} (triangles), and m (squares) and are successively performed, followed by navigation of the cell back to the trap center (arrow) with external fields. Before any UV exposure, the measurement sequences s_n^b are performed to establish a consistent baseline of flagellar output. Afterward, sequential pulses of UV radiation are applied, followed by measurement sequences $s_n^{p_i}$ to assess the effect of the radiation on the flagellar output and to average over stochastic effects. After a series of pulses are collected, the measurement sequence is repeated under constant UV irradiation until the cell is immobilized. This allows the flagellar power output to be plotted against the cumulative UV exposure time (violet line shown in lower graph) as seen in Fig. 5. To see this figure in color, go online.

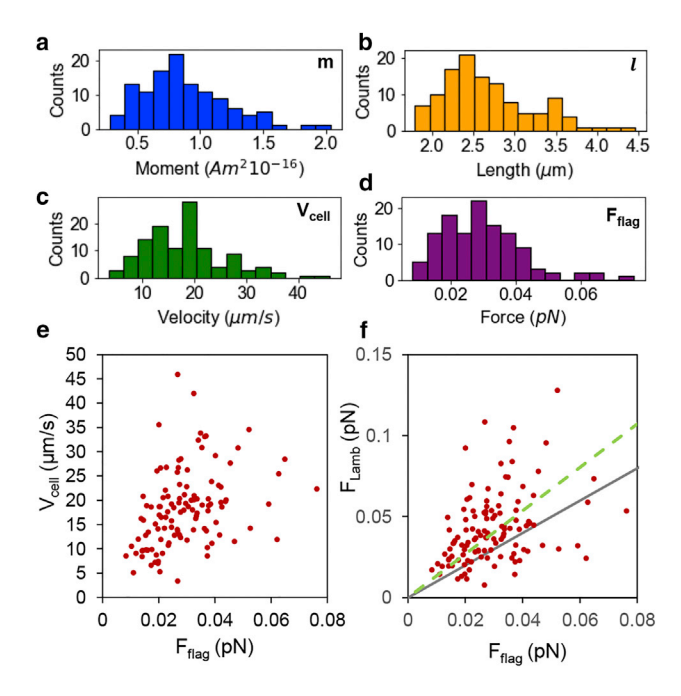


FIGURE 4 Histograms showing distribution of 118 (a) magnetic moments, (b) cell body lengths, (c) swimming velocities V_{cell} , and (d) flagellar thrust measured from launch experiments. (e) Swimming speed V_{cell} versus flagellar thrust F_{flag} is shown for 118 individual cells. (f) Calculated drag force F_{Lamb} on a cylinder at low Reynold's number versus measured thrust force F_{flag} is shown. Solid black line indicates perfect agreement with theoretical calculation of Lamb drag, and green dashed line indicates a linear fit to the data. To see this figure in color, go online.

pN) (37) and Salmonella typhimurium (0.37 pN) (36). These latter bacteria, however, are both peritrichous (multiflagellated), whereas AMB-1 is driven forward solely by a single flagellar motor. The trailing flagellum produces the thrust with counterclockwise rotation while the leading flagellum and body counterrotate (41). Additional possible explanations for the difference between the species could relate to differences in the particular molecular composition of the motors and the properties of the flagellum itself (e.g., length, flexibility).

As noted above, low Reynold's number hydrodynamics predicts the flagellar thrust to be directly proportional to the cell swimming velocity (50) scaled by a geometric factor called the hydrodynamic resistance (51). Indeed, despite significant stochastic effects likely originating in the orientational fluctuations of the bacteria around the angle of the external field θ , Fig. 4 e indicates that V_{cell} and F_{flag} are correlated. A simple estimate of the resistance ($R = F_{flag}/V_{cell}$) of 1.6 fN s/ μ m is roughly an order of magnitude smaller than analogous quantities calculated based on previous studies (25 fN s/ μ m for E. coli (37) and 7.4 fN s/ μ m for E. typhimurium (36)).

Our measurements of F_{flag} display good agreement with an analytical estimate of the drag force on the cell using the linear drag force on a cylinder F_{Lamb} at small but finite Reynold's number, calculated by Lamb (52), as an approx-

imation. This drag force, assumed to be equal to the flagellar thrust because of the low Reynold's number, is given by (52)

$$F_{flag} \approx F_{Lamb} = \frac{4\pi\eta l}{\frac{1}{2} - \gamma - \ln\frac{Re}{8}} V_{cell}$$

$$= \frac{4\pi\eta l}{\frac{1}{2} - \gamma - \ln\frac{dV_{cell}\rho_w}{4\eta}} V_{cell}, \qquad (7)$$

where $\gamma=0.577216$ is Euler's constant, η is the dynamic viscosity of water, l and V_{cell} the measured cell length and velocity, $Re=2dV_{cell}$ (ρ_w/η) is the Reynolds number, d is the cell diameter (taken to be ~ 500 nm from TEM (39)), and ρ_w is the density of water. Fig. 4 f presents the measured flagellar thrust (F_{flag}) versus the calculated Lamb drag (F_{Lamb}) using the measured velocity (V_{cell}) and cell length (l). The solid line indicates the Lamb prediction for a cylinder, and the dashed line indicates a linear best fit to the data, which yields a slope of ~ 1.3 . Thus, the observed drag force ≈ 1.3 F_{Lamb} is roughly 30% larger than that calculated for a cylinder. This increased drag could arise because of the more complex physical shape of the spirochete cell envelope, as well as from the effect of the cell's proximity to the surface during measurement.

It is worth noting that the reported drag observed previously for E. coli is shown to have good agreement with the drag predicted for a prolate spheroid (37), in contrast to our results, which display better agreement with a cylindrical model. For a given cell diameter and length, the cylindrical model presented predicts a drag force roughly an order of magnitude smaller than that of the equivalent spheroid (37), implying that the differences in the observed drag between the species discussed above may be accounted for by shape rather than dimensional factors. We speculate that the higher drag observed on the two peritrichous species likely results from the additional drag created by the presence of multiple flagella distributed randomly over the cell envelope, thereby increasing the effective size of the cell and resulting in better agreement with the spheroidal model. In contrast, the flagella of amphitrichous AMB-1 are positioned solely at the poles of the cell envelope, with the single driving flagellum trailing behind the body and lying along the axis, resulting in better agreement with the cylindrical idealization. These results therefore suggest that the fitness advantage imparted by forming additional flagella may be primarily driven by the need to execute tumbling events that redirect the swimming orientation rather than to attain higher swimming speeds. AMB-1, like many magnetotactic bacteria, is found in vertically stratified oxygen gradients at an oxic-anoxic boundary. Hence, it typically executes a quasi-one-dimensional search for optimal growth conditions, in contrast to the more typical three-dimensional chemotactic search. We therefore further speculate that the differences in flagellar number

may reflect the search space traversed by the cells. Whereas E. coli gains an enhanced ability to sample three-dimensional space by tumbling, AMB-1 generally restricts itself to a one-dimensional search, relying on magnetic orientation to select the appropriate direction.

Flagellar power output

Using the measured thrust F_{flag} and corresponding velocity, the overall power $P = \vec{F}_{flag} \cdot \vec{V}_{cell}$ dissipated by the fluid as a result of the bacterium's swimming can be estimated. Fig. 5 a shows the estimated power of each of the 118 cells plotted against its magnetic moment m, revealing a degree of correlation. Although this correlation is unexpected at first glance, consideration of basic metabolic concerns clarifies the result. Production of the magnetosome chain is highly energy-intensive and is estimated to require 33% of the cell's energy resources (53). Although one might expect that cell length may correlate power consumption and the cell magnetic moment, we do not observe correlation of

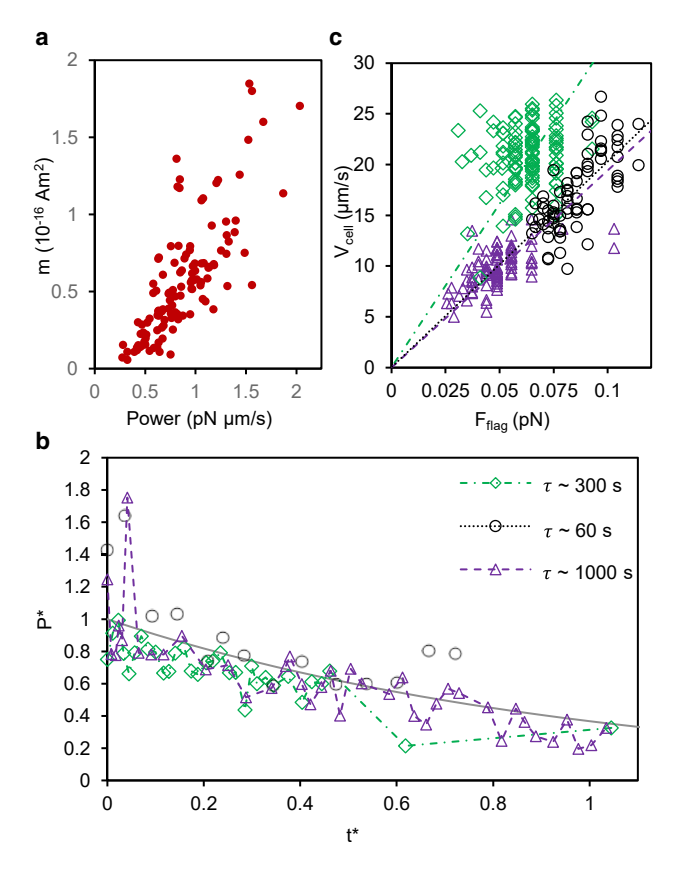


FIGURE 5 (a) Bacterial power output versus measured magnetic moment reveals correlation. (b) Scaled flagellar power output $P^* = P/P_0$ against scaled time $t^* = t/\tau$ is shown for three different cells with time constants $\tau \sim 300$ s (green diamonds), 60 s (black circles), and 1000 s (purple triangles). Solid line indicates exponential curve $P^* = e^{-t^*}$. (c) Experimental flagellar thrust F_{flag} versus velocity V_{cell} for the three AMB-1 exposed to UV radiation that are depicted in (b) is shown. To see this figure in color, go online.

these parameters (see Fig. S1). This lack of correlation may result from the fact that cells used in our study were sampled from multiple batches over a period of several weeks.

The power output of the flagellum, which is ultimately dissipated by the fluid, is an indicator of the availability and efficiency of consumption of energetic resources, serving as a "volt meter" to probe the electrophysiology of single cells, as recently proposed by Krasnopeeva et al. (35). Hence, one expects that higher access to energy sources should yield both higher levels of magnetosome production and correspondingly higher power output from the flagellum, effectively regarding these two processes as a parallel circuit with equal access to metabolic energy resources available to the cell.

Previous work (35,54) has revealed that UV exposure can reduce the flagellar activity of bacterial cells. Although the mechanisms underlying this damage are complex, one identified mechanism implicates the formation of reactive oxygen species (54), which have been shown to result in damage to multiple components of the cell (55,56) (DNA, RNA, proteins, and lipids), including the cell membrane. As the membrane becomes compromised, the osmotic gradient of radicals that power the flagellar motor is reduced, resulting in diminished flagellar power. Indeed, the response of single AMB-1 cells to UV radiation revealed (Fig. 5 b) a quasiexponential decay in flagellar power output (P) as a function of UV exposure with a time constant τ ,

$$P = P_0 e^{-t/\tau},\tag{8}$$

reproducing results consistent with known cell damage mechanisms. Fig. 5 b shows the relative decay in flagellar output power (P/P_0) versus the scaled time $t^* = t/\tau$ for cells with time constants of \sim 60, \sim 300, and \sim 1000 s, respectively. The response to UV exposure of different cells should depend on a number of factors, such as phenotypic variations from cell to cell, the point in the cell life cycle at which the experiment is conducted, and the overall energy resources available to the particular cell. Although these factors were not monitored in our study, the findings demonstrate the ability to track single-cell physiological responses over time. As the flagellar power P drops, the force versus velocity relationship for an individual cell may also be determined (Fig. 5 c) over a range of values, permitting estimation of single-cell hydrodynamic resistance and providing a means of manipulating the single-cell flagellar thrust.

The approach outlined above provides a novel, to our knowledge, and tether-free probe of single-cell energetics that can serve as a foundation for future studies of energetics at the individual cell level. Unlike optical tweezers methods (37), for which single-cell extended time analysis is difficult and parallelization is limited, and invasive surface-tethered cell methods, which require genetic modifications (35), this technique allows unmodified cells to be measured repeatedly for an indefinite duration. Moreover, because the trapping mechanism is based on lithographically patterned materials, the technique lends itself especially to high-throughput studies—the traps may be readily arrayed and integrated with microfluidic environments that isolate cells and allow the chemical environment to be dynamically changed, permitting the direct time-resolved response of large numbers of individual cells to environmental conditions of interest.

Micromagnetic approaches to measuring flagellar thrust are not limited only to the study of inherently magnetic bacteria. Numerous magnetic labeling schemes exist that allow biological material to be rendered magnetic without dramatically altering behavior or hydrodynamics. For example, a chemically functionalized magnetic micelle (\sim 50 nm) (57) has been demonstrated that allows microtubules to be rendered magnetic and remotely controlled (58). For nonspherical cells such as E. coli, random attachment of chemically functionalized magnetic nanoparticles on the cell membrane will result in a net magnetic moment along the cell swimming axis because of the cell's naturally occurring anisotropy. In principle, the measurement of locomotive forces could also be extended to motility strategies such as gliding or undulatory locomotion in nonflagellated organisms or in synthetic microswimmer systems. Furthermore, using appropriately designed magnetic micro-bar magnets, the technique could be scaled up to perform measurements on larger systems such as algae, sperm, or multicellular organisms. Thus, our technique represents a flexible and scalable means of exploring microorganismal motility through application of well-understood physical forces and simple optical detection.

CONCLUSIONS

We have demonstrated a novel, to our knowledge, and facile means of directly measuring thrust and power output of the bacterial flagellar motor in a living microorganism. This technique not only provides a means of exploring the flagellar motor but also allows a unique level of control over the positions of the swimmer in general, thereby extending previous efforts based on optical tweezers and dielectrophoresis via a new, to our knowledge, magnetic mechanism. The mean measured flagellar thrust for AMB-1 is found to be roughly 25 to 15 times smaller than that of the peritrichous bacteria E. coli and S. typhimurium, likely resulting from the relative number of flagellar motors between the species. Our measurements reveal reasonable agreement with a model of the drag coefficient of the spirochete cell envelope, indicating increased drag on the body relative to that of a cylindrical body.

The simplicity of the measurement and the ease with which bacterial trajectories may be controlled make this approach valuable as a probe of single-cell hydrodynamics cell metabolics and as a means of precise microscale manipulation and actuation in bio-driven robotics. Although the technique has been demonstrated on an inherently magnetic organism, the protocol could be extended to various other species of interest through a variety of magnetic labeling schemes that integrate biological materials with designed chemical properties with magnetic nanoparticle systems. In particular, in situations in which relative changes in single-cell thrust in response to environmental changes are required, this approach is especially advantageous; for example, measuring individual cellular thrust and power over time or in response to systematic challenges or differing energy sources. Furthermore, because this technique relies on lithographically patterned traps, it is inherently amenable to multiplexing and hence could be used to rapidly develop statistically meaningful distributions of the properties defining cellular motility.

SUPPORTING MATERIAL

Supporting Material can be found online at https://doi.org/10.1016/j.bpj. 2019.08.036.

AUTHOR CONTRIBUTIONS

C.J.P. designed the experiments, collected and analyzed data, performed calculations, and, along with R.S., drafted the article. E.O. collected and analyzed data and assisted in the numerical fits. E.M. designed and performed the AMB-1 culturing procedures. B.H.L. and S.K.L. designed culture procedures and assisted in the interpretation and analysis of the biological results. R.S. designed the experiments and analysis tools, assisted in interpretation of the results, and supervised the project. All authors evaluated the results and edited the manuscript.

ACKNOWLEDGMENTS

We thank Prof. Fengyuan Yang for the growth of CoFe thin films and Dr. Zachery Oestreicher for the TEM image.

This work was supported by National Science Foundation grants nos. ECCS 1710598 and EAR-1424138.

REFERENCES

- Kallmeyer, J., R. Pockalny, ..., S. D'Hondt. 2012. Global distribution of microbial abundance and biomass in subseafloor sediment. *Proc. Natl. Acad. Sci. USA*. 109:16213–16216.
- Bar-On, Y. M., R. Phillips, and R. Milo. 2018. The biomass distribution on Earth. *Proc. Natl. Acad. Sci. USA*. 115:6506–6511.
- Magnabosco, C., H. L. Lin, ..., T. Onstott. 2018. The biomass and biodiversity of the continental subsurface. *Nat. Geosci.* 11:707–717.
- Flemming, H. C., and S. Wuertz. 2019. Bacteria and archaea on Earth and their abundance in biofilms. *Nat. Rev. Microbiol.* 17:247–260.
- 5. Didelot, X., A. S. Walker, ..., D. J. Wilson. 2016. Within-host evolution of bacterial pathogens. *Nat. Rev. Microbiol.* 14:150–162.
- Coureuil, M., H. Lécuyer, ..., X. Nassif. 2017. A journey into the brain: insight into how bacterial pathogens cross blood-brain barriers. *Nat. Rev. Microbiol.* 15:149–159.
- 7. Davenport, E., J. Sanders, ..., R. Knight. 2017. The human microbiome in evolution. *BMC Biol.* 15:127.

- 8. Ducklow, H. W. 1983. Production and fate of bacteria in the oceans. Biosci. 33:494-501.
- 9. Turley, C., M. Bianchi, ..., F. Van Wambeke. 2000. Relationship between primary producers and bacteria in an oligotrophic sea-the Mediterranean and biogeochemical implications. MEPS. 193:11–18.
- 10. Michaels, A. F., and M. W. Silver. 1988. Primary production, sinking fluxes and the microbial food web. Deep Sea Res. A. 35:473-490.
- 11. Hibbing, M. E., C. Fuqua, ..., S. B. Peterson. 2010. Bacterial competition: surviving and thriving in the microbial jungle. Nat. Rev. Microbiol. 8:15-25.
- 12. Faust, K., and J. Raes. 2012. Microbial interactions: from networks to models. Nat. Rev. Microbiol. 10:538-550.
- 13. Jørgensen, B. 2000. Bacteria and marine biogeochemistry. In Marine Geochemistry. H. D. Schulz and M. Zabel, eds. Springer-Verlag, pp. 173-207.
- 14. Falkowski, P. G., T. Fenchel, and E. F. Delong. 2008. The microbial engines that drive Earth's biogeochemical cycles. Science. 320:1034–1039.
- 15. Fuhrman, J. A., J. A. Cram, and D. M. Needham. 2015. Marine microbial community dynamics and their ecological interpretation. Nat. Rev. Microbiol. 13:133-146.
- 16. Dang, H., and C. R. Lovell. 2015. Microbial surface colonization and biofilm development in marine environments. Microbiol. Mol. Biol. Rev. 80:91–138.
- 17. Berg, H. C. 1975. Chemotaxis in bacteria. Annu. Rev. Biophys. Bioeng. 4:119-136.
- 18. Adler, J. 1975. Chemotaxis in bacteria. Annu. Rev. Biochem. 44:341-
- 19. Wadhams, G. H., and J. P. Armitage. 2004. Making sense of it all: bacterial chemotaxis. Nat. Rev. Mol. Cell Biol. 5:1024-1037.
- 20. Hazelbauer, G. L., J. J. Falke, and J. S. Parkinson. 2008. Bacterial chemoreceptors: high-performance signaling in networked arrays. Trends Biochem. Sci. 33:9-19.
- 21. Sourjik, V., and N. S. Wingreen. 2012. Responding to chemical gradients: bacterial chemotaxis. Curr. Opin. Cell Biol. 24:262-268.
- 22. Bi, S., and V. Sourjik. 2018. Stimulus sensing and signal processing in bacterial chemotaxis. Curr. Opin. Microbiol. 45:22-29.
- 23. Berg, H. C. 2003. The rotary motor of bacterial flagella. Annu. Rev. Biochem. 72:19-54.
- 24. Edwards, M., R. Carlsen, and M. Sitti. 2013. Near and far-wall effects on the three-dimensional motion of bacteria-driven microbeads. Appl. Phys. Lett. 102:143701.
- 25. Zhuang, J., R. Wright Carlsen, and M. Sitti. 2015. pH-taxis of biohybrid microsystems. Sci. Rep. 5:11403.
- 26. Felfoul, O., M. Mohammadi, ..., S. Martel. 2016. Magneto-aerotactic bacteria deliver drug-containing nanoliposomes to tumour hypoxic regions. Nat. Nanotechnol. 11:941-947.
- 27. Ramaswamy, S. 2017. Active matter. J. Stat. Mech. 2017:054002.
- 28. Marchetti, M. C., J. F. Joanny, ..., R. A. Simha. 2013. Hydrodynamics of soft active matter. Rev. Mod. Phys. 85:1143-1189.
- 29. Drescher, K., K. C. Leptos, ..., R. E. Goldstein. 2009. Dancing volvox: hydrodynamic bound states of swimming algae. Phys. Rev. Lett. 102:168101.
- 30. Petroff, A. P., X. L. Wu, and A. Libchaber. 2015. Fast-moving bacteria self-organize into active two-dimensional crystals of rotating cells. Phys. Rev. Lett. 114:158102.
- 31. Pierce, C. J., H. Wijesinghe, ..., R. Sooryakumar. 2018. Hydrodynamic interactions, hidden order, and emergent collective behavior in an active bacterial suspension. Phys. Rev. Lett. 121:188001.
- 32. Wioland, H., F. G. Woodhouse, ..., R. E. Goldstein. 2013. Confinement stabilizes a bacterial suspension into a spiral vortex. Phys. Rev. Lett. 110:268102.
- 33. Wioland, H., F. G. Woodhouse, ..., R. E. Goldstein. 2016. Ferromagnetic and antiferromagnetic order in bacterial vortex lattices. Nat. Phys. 12:341-345.

- 34. Waisbord, N., C. Lefevre, ..., C. Cottin-Bizonne. 2016. Destabilization of a flow focused suspension of magnetotactic bacteria. Phys. Rev. Fluids. 1:1053203.
- 35. Krasnopeeva, E., C. J. Lo, and T. Pilizota. 2019. Single-cell bacterial electrophysiology reveals mechanisms of stress-induced damage. Biophys. J. 116:2390-2399.
- 36. Hughes, M. P., and H. Morgan. 1999. Measurement of bacterial flagellar thrust by negative dielectrophoresis. Biotechnol. Prog. 15:245-249.
- 37. Chattopadhyay, S., R. Moldovan, ..., X. L. Wu. 2006. Swimming efficiency of bacterium Escherichia coli. Proc. Natl. Acad. Sci. USA. 103:13712-13717
- 38. Vieira, G., T. Henighan, ..., R. Sooryakumar. 2009. Magnetic wire traps and programmable manipulation of biological cells. Phys. Rev. Lett. 103:128101.
- 39. Lefèvre, C. T., and D. A. Bazylinski. 2013. Ecology, diversity, and evolution of magnetotactic bacteria. Microbiol. Mol. Biol. Rev. 77:497-526.
- 40. Bazylinski, D. A., and R. B. Frankel. 2004. Magnetosome formation in prokaryotes. Nat. Rev. Microbiol. 2:217-230.
- 41. Murat, D., M. Hérisse, ..., L. F. Wu. 2015. Opposite and coordinated rotation of amphitrichous flagella governs oriented swimming and reversals in a magnetotactic Spirillum. J. Bacteriol. 197:3275–3282.
- 42. Pierce, C. J., E. Mumper, ..., R. Sooryakumar. 2017. Tuning bacterial hydrodynamics with magnetic fields. Phys. Rev. E. 95:062612.
- 43. Li, P., D. Kilinc, ..., G. U. Lee. 2013. Flow enhanced non-linear magnetophoretic separation of beads based on magnetic susceptibility. Lab Chip. 13:4400-4408.
- 44. Frankel, R. B., D. A. Bazylinski, ..., B. L. Taylor. 1997. Magneto-aerotaxis in marine coccoid bacteria. Biophys. J. 73:994-1000.
- 45. Nadkarni, R., S. Barkley, and C. Fradin. 2013. A comparison of methods to measure the magnetic moment of magnetotactic bacteria through analysis of their trajectories in external magnetic fields. PLoS One. 8:e82064.
- 46. Berg, H. C. 1983. Random Walks in Biology. Princeton University Press, Princeton, NJ.
- 47. Smith, M. J., P. E. Sheehan, ..., L. J. Whitman. 2006. Quantifying the magnetic advantage in magnetotaxis. Biophys. J. 91:1098-1107.
- 48. Krichevsky, A., M. J. Smith, ..., M. B. Johnson. 2007. Trapping motile magnetotactic bacteria with a magnetic recording head. J. Appl. Phys. 101:014701.
- 49. Le Sage, D., K. Arai, ..., R. L. Walsworth. 2013. Optical magnetic imaging of living cells. Nature. 496:486-489.
- 50. Purcell, E. M. 1977. Life at low Reynolds number. Am. J. Phys. 45:3-11.
- 51. Kim, S., and S. Karilla. 2005. Microhydrodynamics: Principles and Selected Application. Dover Publications, New York.
- 52. Huner, B., and R. Hussey. 1977. Cylinder drag at low Reynold's number. Phys. Fluids. 20:1211-1218.
- 53. Naresh, M., V. Hasija, ..., A. Mittal. 2010. Synthesis of cellular organelles containing nano-magnets stunts growth of magnetotactic bacteria. J. Nanosci. Nanotechnol. 10:4135-4144.
- 54. de Jager, T. L., A. E. Cockrell, and S. S. Du Plessis. 2017. Ultraviolet light induced generation of reactive oxygen species. In Ultraviolet Light in Human Health, Diseases and Environment. Advances in Experimental Medicine and Biology S. Ahmad, ed. . Springer International Publishing, pp. 15–23.
- 55. Cabiscol, E., J. Tamarit, and J. Ros. 2000. Oxidative stress in bacteria and protein damage by reactive oxygen species. Int. Microbiol. 3:3-8.
- 56. Zhao, X., and K. Drlica. 2014. Reactive oxygen species and the bacterial response to lethal stress. Curr. Opin. Microbiol. 21:1-6.
- 57. Ruan, G., G. Vieira, ..., J. O. Winter. 2010. Simultaneous magnetic manipulation and fluorescent tracking of multiple individual hybrid nanostructures. Nano Lett. 10:2220-2224.
- 58. Mahajan, K. D., G. Ruan, ..., J. O. Winter. 2016. Steering microtubule shuttle transport with dynamically controlled magnetic fields. Nanoscale. 8:8641-8649.